7-2016

Wide Bandgap Organo-lead Trihalide Perovskites for Solar Cells

Miao Hu
University of Nebraska-Lincoln, miao.hu@huskers.unl.edu

Hu, Miao, "Wide Bandgap Organo-lead Trihalide Perovskites for Solar Cells" (2016). *Mechanical (and Materials) Engineering -- Dissertations, Theses, and Student Research*. 101.
http://digitalcommons.unl.edu/mechengdiss/101

Wide Bandgap Organo-lead Trihalide Perovskites for Solar Cells

By

Miao Hu

A THESIS

Presented to Faculty of

The Graduate College at University of Nebraska

In Partial Fulfillment of Requirements

For the Degree of Master of Science

Major: Mechanical Engineering and Applied Mechanics

Under the Supervision of Professor Jinsong Huang

Lincoln, Nebraska

July, 2016

Wide Bandgap Organo-lead Trihalide Perovskites for Solar Cells

Miao Hu, M.S.

University of Nebraska, 2016

Advisor: Jinsong Huang

Methylammonium lead trihalide perovskite ($MAPbX_3$, where MA is methylammonium, and X is a halide)-based solar cells have been extensively investigated recently, with a demonstrated and certified solar power conversion efficiency (PCE) exceeding 20%. To further boost the PCE beyond the Schockley–Queisser limit, tandem structured solar cells have been investigated based on integrating $MAPbX_3$ and the lower bandgap solar cells. Although the best reported efficiency for this type of tandem cells is not close to the theoretically achievable value, mixed-halide perovskite $MAPbBr_xI_{3-x}$ is still one of the most promising candidates as the wide-bandgap light absorber for the tandem application to match the bandgap of silicon, considering its continuously tunable bandgap from 1.6 eV to 2.3 eV with different bromide incorporation ratio. However, the application of the wide-bandgap lead mixed halide perovskite based solar cells has been reported to face several challenges including high intensity of defects, light instability, phase separation, etc. This thesis aims to provide the recent work during my master program involved in the understanding of (1) the characterization of the optoelectronic property of wide-bandgap organolead mixed halide perovskite ($MAPbX_3$), (2) bandgap tunable control of the thin film fabrication process and film post-treatment, (3) device interface and charge transport layers that dramatically influence the efficiency in the $MAPbX_3$ devices, (4) the stability of the $MAPbX_3$ thin films.

ACKNOWLEDGEMENT

First, I would like to express my sincere appreciation to my advisor, Professor Jinsong Huang, who has supported me in my whole master program with his strong expertise and insightful understanding in photovoltaic fields. I thank him for fostering a good and resourceful lab group to conduct research and to receive support from the start of my research career. I have never been more productive in my life than these past two years under his guidance. Through the process of designing the experiments, analyzing the results, writing a peer-reviewed paper, I have learned so much with his patient training. It is his guidance which helped motivate me to explore more and more in this field of study and publish the work we have achieved.

Second, I want to express my special thanks to my master degree committee members, Professor Mehrdad Negahban from the Department of Mechanical and Materials Engineering, and Professor Bai Cui from the Department of Mechanical and Materials Engineering for serving in my master supervisory committee. It is my honor to invite you as my master supervisory committee and I appreciate your valuable comments.

Third, I am grateful to have so many outstanding lab members to work with. In particular, a special thanks to my seniors Dr. Yongbo Yuan, and Dr. Zhengguo Xiao, who have been helping me since I began to work in the lab. Without their help, this work would not have been possible. The communication with them always inspired me to invest in a deeper understanding of each research project. I sincerely appreciate all the others collaborations and help which I have received during my master program.

Finally, I want to express my greatest appreciation to my family. Without their supports and understanding, I would never successfully finish my master degree.

Table of Contents

1 Introduction

1.1 Background and motivation

Wide bandgap organo-lead trihalide perovskites (WBOTP) has been an emerging research area since $CH_3NH_3PbI_3$ was demonstrated to have an outstanding power conversion efficiency (up to 22.1%).[1] The low cost, low temperature, all-solution spin coating fabrication method for organo-lead trihalide perovskites (OTP) thin films enables us to manipulate the formula of the OTP compounds, thus change the cation (X) species in the formulation ABX_3, where A is the methylammonium (MA), B is lead (Pb), and X is halide (Cl, Br, I, or the mix of them).[2-6] It has been shown that the bandgap of the perovskites could be tuned to be wider by changing iodide to bromide or chloride.[7,8] This finding opened a significant potential of WBOTP to be light absorber in tandem device or even lighting and display devices.[8] Fundamental studies of these wide bandgap perovskites are necessary to understand the influence of halide ions in the perovskite structure on the presenting bandgap, which is expected to be precisely tuned into 1.7-1.8 eV for the tandem solar cell applications.[9] [10,11]

Stable PCEs over 20% were successfully achieved by devices with bandgaps around 1.55 eV, however, when it came to $MAPbI_{3-x}Br_x$, whose bandgap is aimed to be 1.7 eV-1.8 eV, inherent problems have been revealed. Firstly, Hoke *et al*. reported that there is a light soaking effect in $MAPbI_{3-x}Br_x$. Incident light induces a halide segregation within the perovskite.[12] The formation of iodide-rich domains with a lower band gap results a sub-gap absorption and a red shift of photoluminescence (PL), thus limits the achievable open circuit voltage for the device with WBOTPs. Furthermore, for this band-gap photoinstability has been one of the biggest challenges of applying $MAPbI_{3-x}Br_x$ in tandem devices. Inspired by his work, I did the photoinstability test to the WBOTP thin films with the optimum bandgap for tandem application with Si, which is 1.72 eV. These films were fabricated within a planar structure. In this thesis, I demonstrate that the photoinstability is directly related to the microstructure and crystal quality of the thin films.

1.2 Experimental Methods

1) Scanning Electron Microscope (SEM)

The scanning electron microscope, also called SEM in this thesis, uses accelerated electrons to hit the sample surface. The energy that is carried by the incident electrons could be dissipated as various signals by the process of electron-sample surface integration, thus delivers the information of the morphology, chemical composition, crystal structure of the solid specimen. The signals that are collected by the SEM for producing image are called secondary electrons. There is another important signal generated at the same time when incident electrons interact with the sample, which is backscattered electrons, often used for analyzing the composition of the sample. The selected areas could range from 1 cm to 1 micrometer, which are all able to be presented in a high resolution image with the conventional SEM techniques. SEM is a very useful technique for material’s morphology identification.

2) X-ray Diffraction (XRD)

Using X-rays to probe crystalline structure has a long history since 1895. X-ray diffraction is still the most efficient and common technique for the study of crystal structures today. When monochromatic X-rays and a crystalline sample have constructive interference, a X-ray diffraction pattern is generated. According to the Bragg's Law, the constructive interference should satisfy the relationship of $n\lambda=2d\sin\theta$, which relates the wavelength of incident X-rays λ to the diffraction angle θ and the lattice spacing *d* in a crystalline sample. By scanning the sample through a range of 2θ angles, all the possible diffraction X-rays are then detected, processed and counted, so that the crystal structure and d-spacing could be concluded by analyzing and indexing the peaks in the X-Ray Diffraction pattern.

3) Photoluminescence (PL)

Photoluminescence is the process that a material emits light after absorbing light. For semiconductors, there are various relaxation forms after photoexcitation. One of them is luminescence or light emitting. By observing the photoluminescence of a semiconductor, we can know the transition energy that is associated with an excited state, which is usually referred to as the bandgap information or the certain excited states (trap states) in the materials.

4) Incident photon to electron conversion efficiency (IPCE)

Incident photon to electron conversion efficiency (IPCE), also referred to External Quantum Efficiency (EQE), is the ratio of the amount of collected charge carriers to the amount of incident photons to the device at a certain wavelength. The process of EQE measurement is conducted by illuminating a certain area of the sample device with a monochromatic light beam and recording the photocurrent generated by the area of the device. The entire IPCE spectrum as a function of wavelength could be obtained by changing the frequency of the incident light.

1.3 Thesis outline

This thesis mainly focuses on enhancing WBOTP device performance by increasing the V_{oc} and by stabilizing the photocurrent output. There are six chapters in this thesis:

In Chapter 1, the research background, research motivation, and organization of this thesis are introduced.

In Chapter 2, the studies I have done relating to the optoelectronic properties of $MAPbX_3$ are introduced. The band structure characterizations including the shape and dispersion of the band edge, exciton binding energy, defects induced by phase separation, are demonstrated to be important for optimizing the photovoltaic device efficiency based on the WBOTPs.

In Chapter 3, the fabrication methods of the WBOTPs thin films are introduced. The highly efficient solar cells require the active layer to be complete and uniform, which makes the fabrication of high quality WBOTPs thin film to be a challenging task. Similar to the fabrication methods of $MAPbI_3$ thin films, the WBOPTs, which are achieved by mixing halide cations in the ABX_3 formulation, could also be obtained by the one-step method and the interdiffusion method, which are commonly utilized in practice. Furthermore, I present our innovative interdiffusion method and post annealing process for fabricating high quality $MAPbI_{3-x}Br_x$ films. Besides of the WBOTPs fabrication, the structure of the $MAPbI_{3-x}Br_x$-based solar cell also varies with individual benefits.

In Chapter 4, the main charge transporting layers utilized in the WBOTP solar cells and their influence on device performance is addressed. Various hole transport materials and electron transport materials are used in the same device configuration to compare the device performance.

In Chapter 5, the stability of the WBOTPs is discussed. Since the wide bandgap of the OTPs is achieved by mixing halide ion in the perovskite structure, it is difficult for the alloy compounds to maintain a stable phase. It has been found that the WBOTPs with an ideal bandgap 1.72 eV is not stable after a certain time period illumination. I will introduce the related research and finding I have done in this chapter.

In Chapter.6, the research effort in this thesis to improve WBOTPs solar cells is summarized. An outlook of this research is also briefly presented in the final chapter

2 The optoelectronic properties of $MAPbX_3$

2.1 Introduction to wide bandgap perovskites

Referred to as the “dye” in dye sensitized solar cell (DSSC) and as the “light harvester” in both mesoporous scaffold structure and planar heterojunction structure solar cells, the optical properties of organolead trihalide perovskite (OTP) has been investigated intensively.[13,2,4] The two crucial characteristics for high performance solar cells, strong optical absorption and efficient carrier transportation are both found in this organic-inorganic hybrid semiconductor.[5,6] However, the photo-generated species have been questioned for a long time.[14] In this section, my related research on the electro-optical properties of OTP materials is introduced, including the dielectric constant, exciton binding energy, exciton dissociation mechanism. Most of the content in this chapter is extracted from my publication “*Distinct exciton dissociation behavior of organolead trihalide perovskite and excitonic semiconductors studied in the same system*”.

2.1.1 Crystal Structure and Phase

With the emerging of WBOTPs, the electro-optical properties of perovskite have been intensively studied, such as the phase transitions, piezoelectric effect,[15] and exciton binding energy. These properties for a general mixed halide perovskite formula $MAPbX_3$ material were reported to have originated from the off-centering displacement of X atoms or a nonpolar rotation of [BX6] octahedra under the strain induced by the replacement of X atoms. In the mixed halide $MAPbX_3$ perovskite structure, different X atoms have different atom radii (6.3288 and 5.6752 Å for X = I and Cl, respectively).[16] Thus, the tilting and rotation of the BX6 polyhedra could occur when different halide ions get into the crystal structure, which directly adjust the bandgap of this material.[16] The rotational motion of the MA cations is illustrated in Figure 2.1.1 by *ab initio* molecular dynamics (CPMD) simulation with the experimental cell parameters.[17,18]

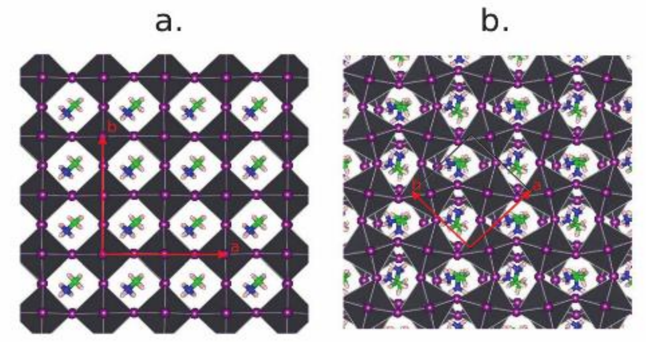

Figure 2.1.1 (a) Cubic model and (b) tetragonal model structures. Highlighted are the employed simulation cells.

$MAPbI_3$ has been confirmed to undergo phase transitions from a tetragonal structure at room temperature to cubic symmetry phase at around 319-327 K.[18,19] Similar temperature dependent phase transition for $MAPbCl_3$ and $MAPbBr_3$ has been reported as well.[19,20] It has been revealed by 1H and 135C nuclear magnetic resonance spectra in methylammonium lead halide perovskites that for OTP materials, $MAPbX_3$, the phase transition is caused by the methylammonium ion reorientation, and the phase sequences are:

$MAPbI_3$: orth.II ($Pna2_1$) to tet.I (I4/mcm) to Cubic (Pm-3m);

$MAPbBr_3$: orth. II ($Pna2_1$) to tet.II (P4/mmm) to Cubic (Pm3m) to tet. I (I4/mcm);

$MAPbCl_3$: Orth. I ($P222_1$)) to tet. II (P4/mmm) to cubic (Pm-3m).

2.1.2 Dielectric Constant

Dielectric is a property of materials that describes the energy that can be stored by the polarization of molecules.[21] When studying this property, it is common to model a material as a capacitor and consider its ability to store charge. Thus, the dielectric constant can be measured as the ratio of the capacitance of a capacitor using that material as a dielectric, compared to a similar capacitor that has vacuum as its dielectric.[22] The dielectric constant is also one essential parameter for OTPs for its photovoltaic effect. It represents the Coulomb interaction between dipoles.[23,24] It is directly related to Coulomb's constant with the relationship $k = 1/4\pi\varepsilon_0$, where k is Coulomb's constant and ε_0 is dielectric constant. The MA ion has a permanent electric dipole moment, which could experience an extremely rapid overall reorientation along C-N axis in a perovskite structure. This dynamic dipole moment orientation changing is expected to contribute to the dielectric properties of the substance.[24] With a compositional engineering based on halide composition of thin films and single crystal, dielectric permittivity of $MAPbX_3$ (X is Cl, Br, I or the mixture of them) have been experimentally measured with a wide frequency range by several methods, including optical absorption, magnetoabsorption[25], impedance analyzer, and etc. However, due to the challenge of fabricating thick, uniform, pinhole-free thin films for mixed halide perovskite, prior work has focused on iodide perovskite. This prior work is outlined in the remainder of this section.

A widely recognized value for the real part of static dielectric constant was given to be about 70 for bulk $MAPbI_3$ by Lin *et al*. in 2014.[23] This value was obtained by measuring the optical constants (refractive index n and extinction coefficients k) for all the layers in perovskite-based planar devices in a wide range of frequency ranges from (20 Hz-

40 MHz).The results are shown in Figure 2.1.2, and the relative dielectric constant is given by the simple relation:

$$\varepsilon' = n^2 - k^2 \,, \varepsilon'' = 2nk \qquad (1)$$

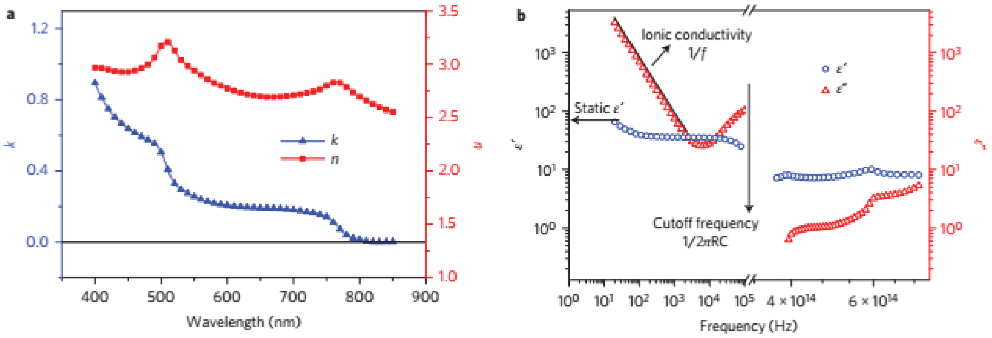

Figure 2.1.2 (a) Optical constants of the $CH_3NH_3PbI_3$: refractive index (n) and extinction coefficient (k), as determined by employing spectroscopic ellipsometry, near-normal incidence reflectance and total transmittance. Three different spectral regions occur: $\lambda > 800$ nm with minimal absorption, 500 nm $< \lambda < 800$ nm with moderate absorption (comparable with the absorption of typical organic semiconductors) and $\lambda < 500$ nm with the very strong absorption characteristics from PbI_2. b, Dielectric constants of $CH_3NH_3PbI_3$, real and imaginary parts, in the optical (high) frequency regime as determined from n, k and low-frequency and static values from impedance analysis and CELIV, respectively. A high static dielectric constant of ~70 is notable. The 1/f behavior of the imaginary part of the dielectric constant is indicative of the ionic nature of this perovskite.[23]

In my own experiments, I observed a similar relative dielectric constant value ranging from 50-100 at low frequencies. I obtained the relative dielectric constant of the $MAPbI_3$ thin films with impedance spectroscopy, which measures the capacity with frequency ranges 0.01 Hz to 1000 Hz. Surprisingly, the dielectric constant of $MAPbI_3$ thi-film was barely studied until recently, which might be due to the difficulty to form the pin-hole free perovskite thin films. A recent study of dielectric response of $MAPbI_3$ was executed on devices containing multiple layers including mesoporous or compact electrodes,[9] and thus did not measure the dielectric property of the perovskite layer itself exclusively. In this thesis, I applied a recently developed interdiffusion approach to form the continuous, leakage-free perovskite thin films.[26] This pinhole-free 1um $MAPbI_3$ film, whose surface and cross section scanning electron microscope images are shown in Figure 2.1a and 2.1b, give us the opportunity to study the dielectric properties of this single layer material. The perovskite films were deposited on poly(3,4-ethylenedioxythiophene):poly(4-styrenesulfonate) PEDOT:PSS covered indium tin oxide (ITO) or bare ITO substrates, and were covered by gold electrodes with a simple device structure as shown in the inset of Figure 3c. The frequency dependent dielectric constant of the devices were measured in dark conditions at zero bias to avoid any poling effect. A large dielectric constant over 500 was observed on a low frequency of 20 Hz, which is lower than the dark dielectric constant of over 1000 reported by *J. Bisquert*.[27] The discrepancy can be explained by the different device structure used because charge trapping and detrapping in the nanocrystalline TiO_2 film can cause a huge dielectric response in the low frequency range. This also indicates the importance to differentiate the dielectric response from that of other layers using a single layer perovskite film. As we can see, the relative dielectric constant is about 32 at high frequencies, consistent with that measured by *A. Poglitsch* with a dispersive polarizing millimeter-wave interferometer.[28]

Such a large relative dielectric constant indicates that $MAPbI_3$ is a non-excitonic material, as the Coulomb interaction between electron and hole pairs can be effectively screened.

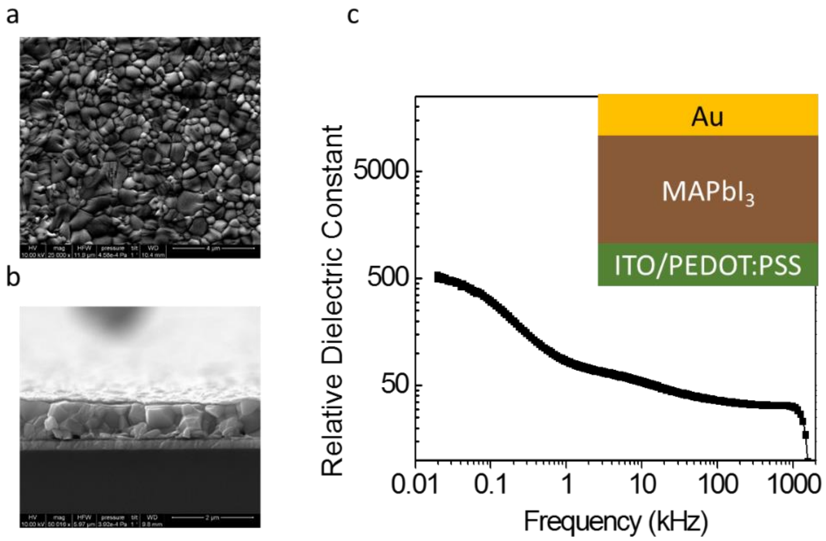

Figure 2.1 (a)(b) top view and cross section SEM images of the perovskite thin films prepared in interdiffusion method. (c) Frequency-dependent dielectric constant of the $MAPbI_3$ film. The device structure of $MAPbI_3$ film for dielectric constant measurement is shown in the inset.

2.2 Exciton or free charge

The concept of photogenerated species of OTP is hotly discussed topic. On the one hand, it is a common observation that an exciton absorption peak appears at the edge of optical absorption cut-off with an increasing bandgap.[14,29,30] On the other hand, the large dielectric effect in OTP discussed above suggests the dielectric screening must be large to form exciton. The excitonic optical property indicates that OTP is possibly an excitonic material, then the exciton dissociation and charge collection might be one of the major reasons for energy loss. It follows that the exciton binding energy is significant for estimating the energy loss, and is also beneficial for the light emitting studies of WBOTPs.

2.2.1 Optical Absorption of WBOTPs

The optical absorption of a photovoltaic semiconductor is essentially the process of elements transitioning between valence band (VB) states and conduction band (CB) states, which in particular materials, is also determined by density of states (DOS).[31] Therefore, the optical absorption coefficient of a material is closely related to its electronic structure. OTPs are attractive photovoltaic materials because OTPs have strong optical absorption, which means the required thickness and the challenges in collecting photogenerated carriers could both be reduced. The relatively high exciton binding energy compared to those of III–V semiconductors with a similar bandgap (37–50 meV have been reported for iodide in the low-temperature phase[16] and 35–75 meV for the mixed chloride at room temperature[14]), not only lowers the absorption threshold, but also increases the strength of the above-bandgap absorption that generates unbound electron–hole pairs.

For OTP single crystals, the $MAPbI_3$ and $MAPbBr_3$'s exciton binding energy has been predicted respectively to be 45 meV and 70 meV at low temperature, indicating a Wannier-Mott type exciton. For the OTP polycrystalline thin film, by measuring the full width at half-maximum of the exciton absorption peaks,[32] the exciton binding energy was estimated to be 80 meV for $MAPbBr_3$ and 87 meV for $MAPbBr_{3-x}Cl_x$, both of which are larger than that of $MAPbI_3$ (19~56 meV). Another reported method is using high magnetic fields inter-band magneto-absorption to obtain a spectroscopic measurement of the exciton binding energy, which is found to be only 16 meV at low temperatures.

2.2.2 Exciton Dissociation Mechanism

Excitons are the photogenerated electron-hole pairs, and can be classified into two types, Wannier exciton and Frenkel exciton. In Wannier excitons, the Coulomb interaction of electron-hole pairs is small, thus results in a large electric field screening length. Wannier excitons have weak bonding energy of 0.01 eV, and can be easily separated.[33,34] Theoretically, the generated free charges are able to be extracted out under the built-in electric field in the p-n junction solar cells. However, most organic semiconductors have a relatively small dielectric constant, resulting a strong Coulomb interaction between the photogenerated electron-hole pairs, whose binding energy could reach between 0.1-1 eV.[33] This type of excitons are referred to as Frenkel excitons. The thermal activation at room temperature can no longer dissociate this type of excitons, such that an external electric field or the internal electric field induced by the band offset is needed to separate them.

For MAPbX (X is Br or Cl or mixture of them), the exciton dissociation dynamics was studied by comparing the electric field dependent incident photon to charge carrier efficiency (IPCE) of MAPbX and the conventional excitonic semiconductors in the same device. The exciton generation and dissociation were studied extensively in organolead bromide and organolead bromide-chloride mixed halide perovskites, which might have a larger exciton binding energy due to a larger bandgap. To find out whether these large binding energy excitons can be dissociated and contribute to the photocurrent in Br and Cl based perovskite devices, we measured the wavelength dependent photocurrents of the corresponding devices by IPCE. Figure 2.2.1 shows the EQE curves of the devices based on the four types of perovskite thin films, with the device structure of ITO/PEODT:PSS/$MAPbX_3$/PCBM/C_{60}/BCP/Al. The EQE peaks are consistent with the exciton absorption peaks, demonstrating that the excitons generated in mixed halide perovskite could be efficiently dissociated despite the large exciton binding energy over 80 meV. [13]

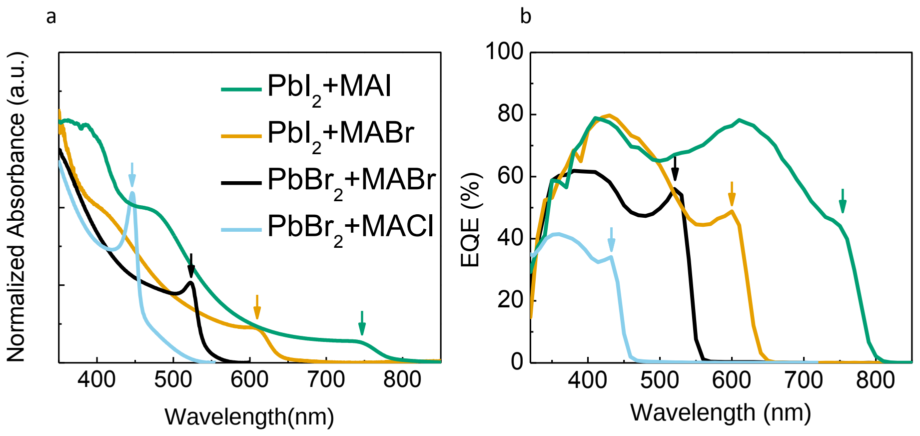

Figure 2.2.1 (a) Normalized absorption of perovskite film fabricated from varied precursors, showing a blue shift with addition of Br and Cl. (b) EQE of devices built on the corresponding perovskite films

Since $MAPbBr_3$ has a larger bandgap than C_{60}, its absorption and EQE spectrum band can be separated from that of C_{60}, which allows for the study of the electric field dependent exciton dissociation behavior of these two materials in a single device. We expect to see a fundamental difference between excitonic materials and non-excitonic materials on the electric field dependent charge generation. For non-excitonic materials, free charges are generated upon light absorption, thus the electric field has no effect on charge generation yield; while for excitonic materials, the excitons with large binding energy need to be dissociated either by a large energy offset at the donor-acceptor interface or by a strong electric field that draws the electron and hole apart. The field-dependent dissociation rate, k_{D} can be described quantitatively by the Onsager model.[35-37]

$$k_{\mathrm{D}}(E) = k_{\mathrm{R}}\frac{3}{4\pi a^3}e^{-E_{\mathrm{B}}/kT}\left[1 + b + \frac{b^2}{3} + \frac{b^3}{18} + \frac{b^4}{180} + \cdots\right] \qquad (2)$$

where k_R is the bimolecular rate constant of the bound electron hole pair (e-h pair), a is the initial separation of the bound e-h pair at the interface, $b = e^3E/8\pi\varepsilon_0\varepsilon_r k^2T^2$, ε_0 is the dielectric permittivity of the vacuum, ε_r is the relative dielectric permittivity of the active layer, and EB is the e-h pair's binding energy. According to the Onsager model, field-dependent dissociation rate cannot be predicted by materials' intrinsic parameters, such as exciton binding energy or dielectric constant exclusively. In order to examine this dynamic property, we continued to test the external electric fields dependent EQE of $MAPbBr_3$ devices with structures of ITO/PEDOT:PSS (30 nm)/$MAPbBr_3$ (100 nm)/PCBM/C60 (200 nm)/BCP (80 nm)/Al (100 nm) and ITO/PEDOT:PSS (30 nm)/$MAPbBr_3$ (100 nm)/spun ICTA/ evaporated ICTA (200 nm)/BCP (80 nm)/Al (100 nm). Here there is a possibility that ICTA may decompose into PCBM or other fullerenes derivatives, however, the spun layer of ICTA maintained its composition on the perovskite thin film during the whole process. Since the LUMO level of ICTA is not lower than that of $MAPbBr_3$ (Figure 2.2), the existence of ICTA excludes the situation that the inner electric field offered by the LUMO offset between $MAPbBr_3$ and ICTA could assist the dissociation of photoinduced excitons.[13]

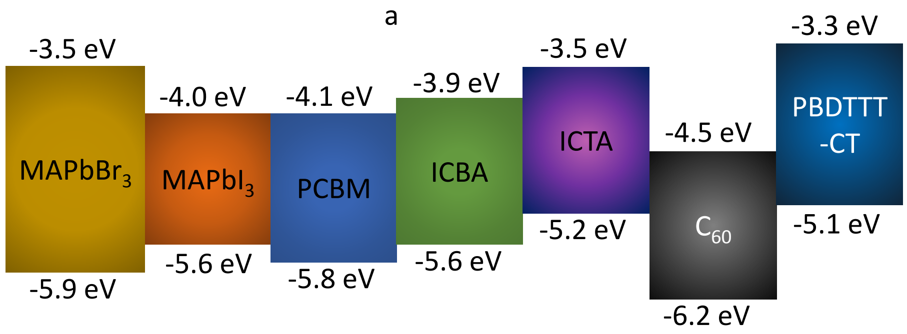

Figure 2.2 Energy levels of $MAPbI_3$, $MAPbBr_3$, various fullerenes, and PBDTTT-CT

As shown in Figure 2.2.1a and b, the devices have a reasonably high EQE of around 60% in $MAPbBr_3$'s absorption spectral range at zero bias. While the EQE in the absorption band of 560 nm-750 nm, where only PCBM, C_{60} or ICTA absorbs, is close to zero. This indicates that the photoinduced charge transfer from PCBM, C_{60} or ICTA to $MAPbBr_3$ is negligible, excluding the possibility that band offset exits at $MAPbBr_3$/PCBM, or $MAPbBr_3$/ICTA interface. With a gradually increasing external electric field up to $0.8\times 10^5\ V/cm$ (4 V applied on approximate 500 nm device), the EQE in the $MAPbBr_3$ absorption band remains unchanged during the whole process, but increases dramatically by 4 to 5 times in the PCBM, ICTA or C_{60} absorption band. We infer that the generated excitons in $MAPbBr_3$ have obtained a nearly maximum dissociation efficiency even without an external electric field or an energy level offset at the heterogeneous interface. However, few excitons generated in PCBM, ICTA or C_{60} dissociated into free charges to contribute to the photocurrent unless a large reverse bias was applied. The reason is that the absorbed sunlight in the 560~750 nm wavelength range can yield photocurrent only from Frenkel exciton dissociation, since the bandgap of charger transfer excitons (CTEs) in fullerene of ≈2.3 eV is too larger.[38,39] CTEs are formed by delocalized electrons transfer between the fullerene molecules, which is considered to be responsible to the photocurrent yield from fullerenes based Schottky junction device.[40,41] This result verified the field independent exciton dissociation in $MAPbBr_3$ and field dependent exciton dissociation in fullerenes, providing another piece of evidence for the non-excitonic nature of $MAPbBr_3$ despite having larger exciton binding energy than $MAPbI_3$.

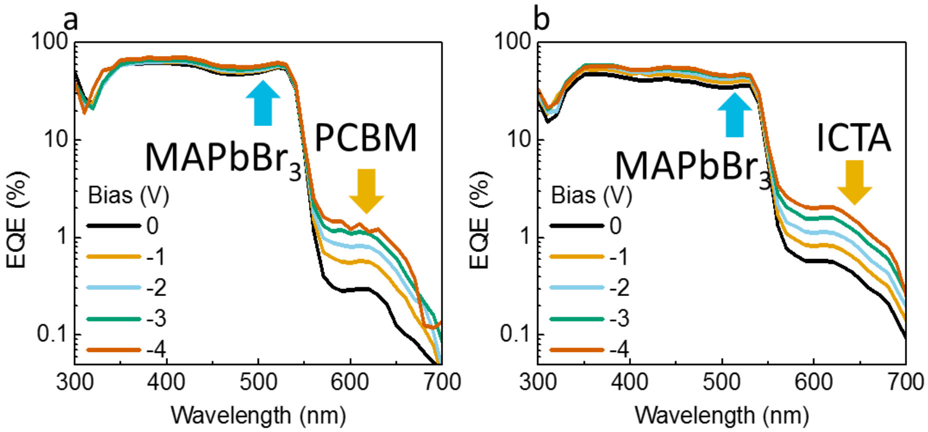

Figure 2.2.2 EQE spectra of the $MAPbBr_3$ devices with different electron collection layers of a) PCBM and b) ICTA under the increasing reverse bias from 0 to −4 V; EQE signals between 560 and 700 nm are contributed by fullerenes

It was observed that the excitons could achieve a maximum dissociation in $MAPbX_3$ without any external field or a heterogeneous interface acting on it, while exciton dissociation in excitonic materials was strongly field dependent. The results indicate that OTP photovoltaic cells should be treated as traditional inorganic thin film photovoltaic devices, rather than organic or hybrid ones.

To summarize, this chapter first presents the optical absorption for OTPs. Then introduced the excitonic absorption peak found in wide bandgap OTPs. The topic of the excitonic nature of this hybrid material subsequently is discussed by the individual studies of the dielectric measurement, ETL dependent open circuit voltage examine, and electric filed dependent IPCE measurement. Eventually, it could be concluded that even though $MAPbBr_3$ or mixed halide perovskite have relatively large exciton binding energy in excess of 80 meV, they still should be treated as nonexcitonic semiconductors.

3 Bandgap tunable control of the thin film from fabrication process

3.1 Motivation to study bandgap engineering in OTP thin film fabrication

Organal-lead trihalide perovskites (OTP) have attracted intense research interest recently, not only because the outstanding high power conversion efficiency, but also because the tunable bandgap by mixing different ratio of halide (Cl/Br/I). This fantastic character enables versatile significant applications of perovskite materials in light emitting devices, lasers, photodetectors. Moreover, the tunable wide bandgap perovskites are also required in the photovoltaic application considering spectrum broadening with another bandgap matching light absorber.[42] In this chapter, I will show that OPT compounds are very tolerant to stoichiometric adjustment of halide synthesis. Recent studies on the wide bandgap perovskites also concerns the substitution of the organic component from methylammonium (MA) to formamidinium (FA), which allows more structural capability of different anions. The bandgap tunability has been found to be the direct result of anion substitution in the perovskite structure, which predicts a potential of phase separation with the certain stimuli existence, which will be discussed later along with the stability of WBOTP. I will also introduce the low temperature fabrication method for wide bandgap perovskite thin films, which is a main contribution of this thesis.

3.2 Bandgap Tuning

3.2.1 The target bandgap for Si based tandem application

It is well known that to exceed the Shockley-Queisser limit for the efficiency of solar cells, tandem devices with complementary absorption spectra are necessary to increase the absorption of sunlight over a wide range of wavelengths while minimizing thermodynamic loss in individual cells. Crystalline-Si (c-Si) technology produces excellent single junction solar cells with conversion efficiencies of 24-25%, and have been commercialized extensively to produce panels at relatively low costs.[9] To produce efficient tandem cell with c-Si, WBOPTs have two basic requirements: first it needs to be deposited inexpensively on c-Si, and second it must have a bandgap match with c-Si (1.12 eV) in a tandem cell, which needs to be tuned a bandgap of 1.72 eV to produce ~20 mA/cm^2 short circuit current density (J_{SC}) under air mass (AM) 1.5 spectrum, which can potentially produce high device efficiency above 30%.[43] These requirements can be met by using the recently developed organometal trihalide perovskite materials.

3.2.2 Bandgap engineering by exchanging halide ion in OTPs

As mentioned before, one of the advantages of hybrid organometal trihalide perovskite (OTP) materials for photovoltaic application is its bandgap can be continuously tuned between 1.17 eV to 3.11 eV by manipulating the ABX3 components. The main topic of my work during my master program involved studying incorporating varied halide (Cl, Br and I). However, there are also some recent studies which show that changing organic ions might be another way to enlarge bandgap of OTPs or even substituting the organic ions (A from ABX_3) with metal ions.[5,7,11] Snaith *et al.* recently published work suggesting that Cs+ could be used instead of CH3NH3+, thereby potentially eliminating the issues of instability which commonly existing in the WBOPTs. However, prior to this finding, the bandgap of perovskite was tuned to be 1.72 eV by using lead iodine/bromine (PbI_2/PbBr2) layers first spun on the indium tin oxide (ITO)/HTM substrate from dimethylformamide (DMF) solution, and then CH_3NH_3Br (MABr); CH_3NH_3I (MAI) blended precursor solution with different blend ratios were spun on the top of the first inorganic layer.

Perovskite's bandgap can be linearly tuned by manipulating the MABr percent in the blend precursor solution. Figure 3.2.2 shows the absorption curves of perovskite films fabricated in this way, where we can see a continuous blue shift of the absorption cut-off with increased Br percent in precursor.

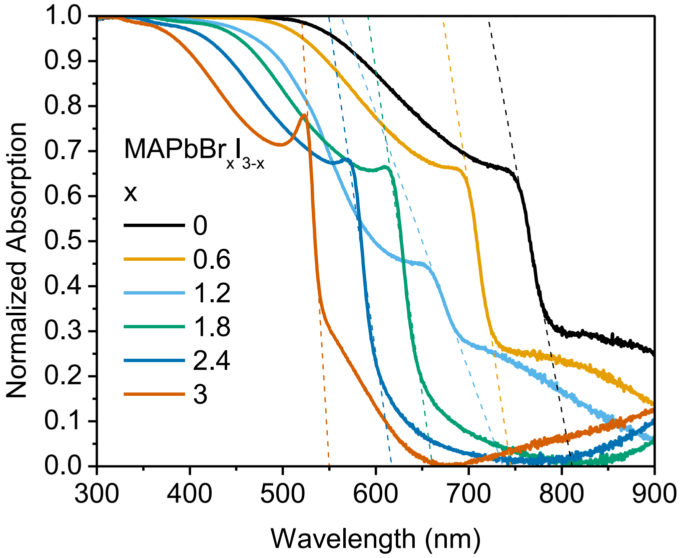

Figure 3.2.2 optical absorption of films grown from varied MABr percent in the MABr: MAI blended precursor solution

In this chapter, I briefly introduced the methods that are used in the highly efficient wide bandgap solar cells. With this mixing halide method, the bandgap could be easily tuned with the similar fabrication routine that is utilized in making $MAPbI_3$ thin films, which translates to a maintainable and low cost on procedure for industrial levels6.

4 Device interface and charge transport layers

A good device does not only require the delicate control of the quality of each layer, but also needs comprehensive engineering of the device interface because it is indicative of the whole charge transport dynamics through the device. In the previous chapter, perovskite layer fabrication was discussed. Subsequently, the choice of the charge transport materials which are compatible with OTPs must be considered. Such material must be able to efficiently extract charges thereby reducing the recombination inside the absorber. This section summarizes the electron transport layer (ETL) and hole transport layer (HTL) materials that I have used in highly efficient WBOTP solar cells in my master program. Most of the content in this chapter is extracted from my publication "*Stabilized Wide Bandgap MAPbBrxI3–x Perovskite by Enhanced Grain Size and Improved Crystallinity*"

4.1 Hole transporting layer

Generally, HTL materials utilized in WBOTP devices can be small molecules, polymers and inorganics, as long as its highest occupied molecular orbital (HOMO) level matches to WBOTP`s HOMO. Spiro-OMeTAD is one of the most widely-used small molecule HTLs in both mesoporous and planar perovskite solar cells, however, dopants have to be used to in Spiro-OMeTAD due to its low mobility. An improved conductivity is achieved by adding dopants in the Spiro-OMeTAD solution before spin coating, PEDOT:PSS is another widely used HTM in planner structured devices with a work function of 5.0 eV. However, the energy-level misalignment between PEDOT:PSS's work function (5.0 eV) and valence band of $MAPbI_3$ (5.46 eV) is assigned to be responsible for the lower device V_{OC}. It should be noted that the high work function of HTL does not guarantee the large device V_{OC} as the small perovskite grains grown on the wetting HTL lower the V_{OC} through the stronger charge recombination at the grain boundaries as we discussed before in 3.3. This is because the energy level of HTL might not limit the Fermi energy splitting of the device under illumination.

In my program, non-wetting HTLs including c-OTPD and PTAA was used to grow large aspect ratio perovskite grains. Figure 4.1a shows the I-V curve of an optimized $MAPbBr_{0.8}I_{2.2}$ cell with the device structured with ITO/ PTAA/ $MAPbBr_xI_{3-x}$/ [6,6]-phenyl C_{61}-butyric acid methyl ester (PCBM)/ C_{60}/ 9-dimethyl-4,7-diphenyl-1,10-phenanthroline (BCP)/ Al, in which the device parameters can be derived as a J_{sc} of 15.8 mA/cm^2, a V_{oc} of 1.21 V, a FF of 78%, and the PCE of 15.0%. The negligible hysteresis of the device indicates a low trap density of the active layer $MAPbBr_{0.8}I_{2.2}$ formed by the interdiffusion method.[44] The selected hole transport layer PTAA is employed in this work, with the initial intention to lower the HOMO to -5.20 eV in order to reduce the energy loss.[45,46]

Besides of this, we observe that PTAA thin film is hydrophobic to the precursor`s solvent DMF, which results a higher contacting angle between perovskite and the substrate. According to the solid nucleation mechanism, the Gibbs free energy barrier for nucleation (ΔG_{het}) could be determined by the contacting angle with the relationship:

$$\Delta G_{het} = \Delta G_{hom}(2 + cos\theta)(1 - cos\theta)^2/4, \qquad (3)$$

where ΔG_{hom} is homogeneous nucleation energy barrier.[47] When θ approaches 180°, ΔG_{het} gets maximum, suppressing the nucleation process and nuclei`s population, thus large grains could form from less density of nuclei distributed in a same device area.[48]

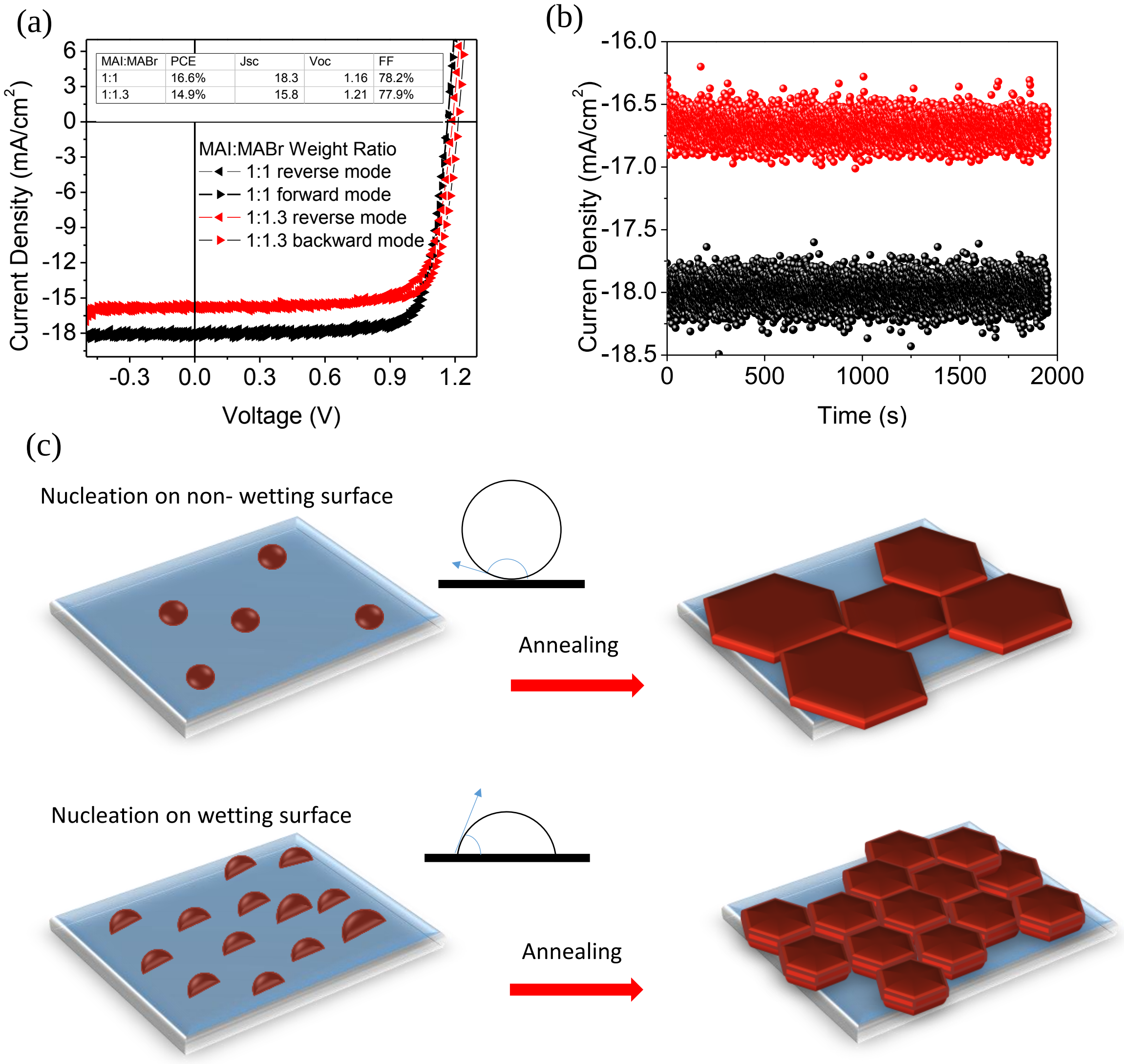

Figure 4.1 (a) *J-V* curves for optimized solar cells with various thickness of $MAPbBr_{0.8}I_{2.2}$; (b) Photocurrent measured for 20 min at the maximum power output point for the two devices corresponding to (a); (c)Schematic illustration of nucleation and growth of grains on wetting and non-wetting hole transport layer surface and the corresponding cross-section SEM images, for 328 nm thick $MAPbBr_{0.8}I_{2.2}$ thin film grown on a) PTAA, b) 361 nm thick thin film grown on PEDOT:PSS, c) 540 nm thick $MAPbBr_{0.8}I_{2.2}$ thin film grown on PTAA

4.2 Electron transporting layer

Generally, ETL materials utilized in WBOTP devices could be inorganic and organic n-type semiconductors. TiO_2 is one of widely used ETLs in both mesoporous scaffold architecture and compact architecture because it does not react with perovskite materials and its high electron mobility which could reduce the recombination in the device while working. However, TiO_2 could be only produced under high temperature, which also requires to the transparent electrode substrate to be high temperature resistance. So indium tin oxide (ITO) must be substituted with fluorine-doped tin oxide (FTO), which adds the cost of the device. Another well-accepted ETL is fullerene derivatives, which could be spun on the top of perovskite layer in a solution under low temperature.[16] This structure avoids using high temperature to fabricate the mesoporous TiO_2 layer as the electron transport layer. It was also found that PCBM has an additional passivation effect on grain boundaries and surface of the perovskite layer because inserting PCBM was found to be responsible for the reduction of the total trap densities and elimination of the photocurrent hysteresis.[17] Considering that the various energy level of fullerene derivatives would impact the electron transferring from $MAPbI_{3-x}Br_x$ into them, it is studied different fullerene layers including PCBM, indene-C_{60} tri-adducts (ICTA) and indene-C_{60} bisadduct (ICBA) in the same $MAPbI_{3-x.}Br_x$ device configuration. Figure 4.2(a-d) show the *J-V* curves of the devices using different fullerene derivative layers with increasing and decreasing bias. The photocurrents were measured at a rate of 0.06 V/min under AM 1.5 illumination. It was found that both PCBM and ICTA can effectively passivate the $MAPbI_{3-x}Br_x$ films, resulting a PCE larger than 12.0 %, J_{SC} of 17.0-17.5 mA cm^{-2} and *FF* of 70.0%, while ICBA or no spun fullerene passivation overall yield a lower PCE with smaller J_{SC}, reduced *FF* and significantly decreased V_{OC}. Nevertheless, it is noted that only PCBM passivated device shows no photocurrent hysteresis when changing the current sweep direction (Figure 4.2a), while ICTA sample, though shows the similar PCE, was observed hysteresis with lowered J_{SC} and *FF*. The similar observation was also found in the ICBA and the no fullerene samples. The hysteresis observed here may come from the insufficient passivation on charge traps in perovskite films.[16,17]

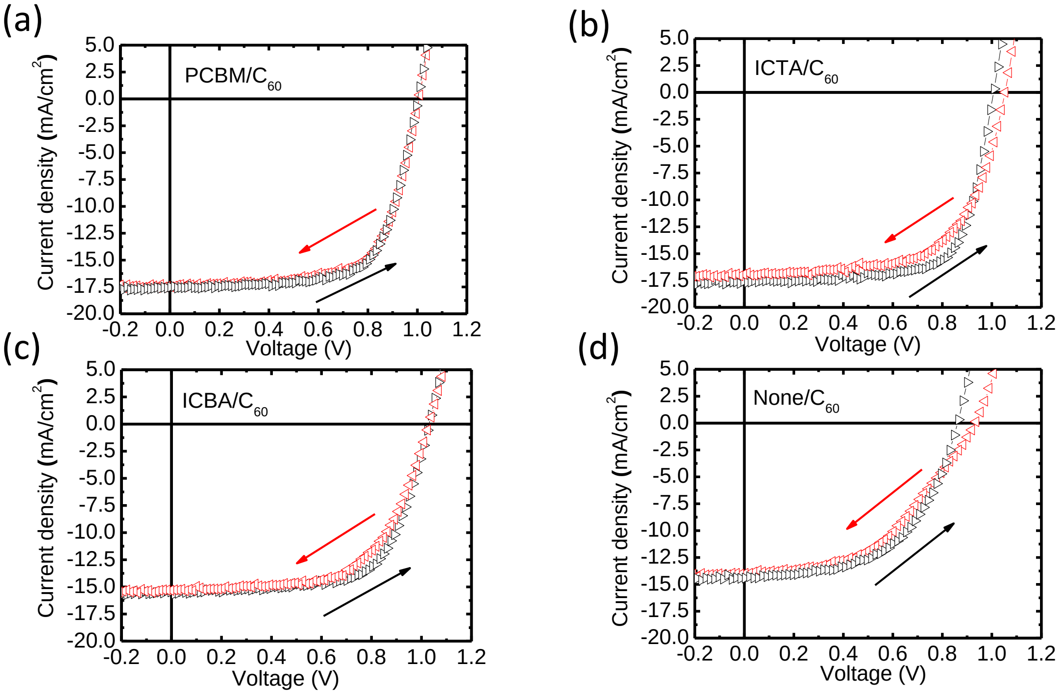

Figure 4.2 J–V curve of the $MAPbI_{2.4}Br_{0.6}$ devices with PCBM, ICTA, ICBA, and without fullerene derivative passivation, respectively.

In this chapter, the hole transport materials and electron transport materials that could be employed in the inverted planar structure of perovskite solar cells were introduced with device performance data presentation. Except from the benefit of all-solution, low temperature process, we also found the usage of PCBM as ETL in perovskite solar cells could suppress hysteresis. This does not only enhance our device performance, but also reveals a new direction on the passivation study of the OTPs.

5 Stability of the $MAPbX_3$ thin films

5.1 Challenges to apply WBOTPs in tandem devices

Intensive effort has been made to integrate WBOTPs into the tandem structure, however, the best reported efficiency of this type of tandem cell is still limited by the top cell`s stability. The mixed halide perovskite $MAPbBr_xI_{3-x}$ was employed in this device as the wide bandgap light absorber to match the bandgap of silicon/CIGS, considering its continuously tunable bandgap from 1.6 eV to 2.3 eV with the increasing bromide incorporation ratio.[49-51] However, the application of $MAPbBr_xI_{3-x}$ based solar cells has been reported to confront with one big challenge of intrinsic photo-instability. The $MAPbBr_xI_{3-x}$ material was shown to be unstable under illumination in the devices with the mesoporous scaffold. A phase separated into two phases, one iodine rich phase and one iodine pure phase. [52,53] The low bandgap phase thus acts as charge trap, which was hypothesized to severely reduce device`s open circuit voltage and PCE.[46,54-56] In this section, I will introduce a photoexcitation stable $MAPbBr_{0.6}I_{2.4}$ mixed halide perovskite, which has a optical bandgap of 1.72 eV. An increased grain size and an improved crystallinity have been identified to be responsible for the enhanced photostability of the $MAPbBr_xI_{3-x}$ mixed halide perovskite. Most of the content in this chapter is extracted from my publication "*Stabilized Wide Bandgap MAPbBrxI*$_{3-}$*x Perovskite by Enhanced Grain Size and Improved Crystallinity*"

5.2 Microstructure of the thin film based on the wettability of the substrate

According to the comparison of PTAA and PEDOT:PSS as the HTMs served in perovskite solar cell in Chapter 4, we found that the device built on PTAA has a very stable photocurrent output in a 30-min long period. To determine whether the larger grains and better crystallinity of the films contribute to the high efficiency and the light stability, I did another comparison study on the thickness of the WBOTPs. The control for the substrate surface energy to the grain growth could only apply the restructuration to the near bottom area,[57] so it is reasonable to speculate that a thicker polycrystalline film might loss the arranged crystallization. This hypothesis is confirmed by the cross-section SEM images. In Figure 5.2 (a) the clear and neat grain boundaries go thoroughly from bottom to the top in the 320 nm $MAPbBr_{0.8}I_{2.2}$ thin film. However for the 540 nm $MAPbBr_{0.8}I_{2.2}$ thin film (Figure 5.2 (b)), the randomly chosen cross-section areas are relative ordered in a 3-um scale, but contain numerous stacking little grains if looking into.

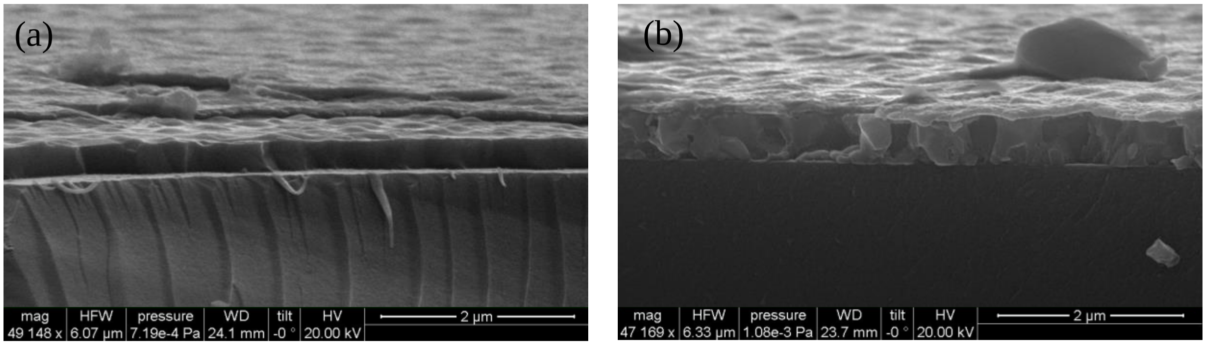

Figure 5.2 Cross-section SEM images, (a) for 328 nm $MAPbBr_{0.8}I_{2.2}$ thin film grown on PTAA, (b) for 540 nm $MAPbBr_{0.8}I_{2.2}$ thin film grown on PTAA

5.3 The influence of WBOTPs microstructure on device performance

After confirming that the microstructure is also determined by the thickness of perovskite thin film, I then built a series of cells based on the certain composition of $MAPbBr_{0.8}I_{2.2}$ with different thickness. The cells` *J-V* curves are shown in Figure 5.3a with an arrow to illustrate the thickness increasing trend, in which the device performance derogates with the thickness increasing. Considering the fact that the device structure and the perovskite composition are the same among this set of cells, we suspect that the worse device performance may come from the microstructure dependent photoexcitation phase separation in bromide and iodide mixed perovskite. The compositional phase separation existence in mixed halide perovskite was also observed by R. H. Friend`s group with a study showing that aging of the $MAPbBr_xI_{3-x}$ can cause an automatic separation between I-rich region and Br-rich region.[53] Then M. D. McGehee`s group also reported a similar phenomenon of phase separation in the mixed halide perovskite introduced by photoexcitation.[52] In my study, the $MAPbBr_xI_{3-x}$ with the bandgap of 1.72 eV contains 27.5% bromide, over the 25%, which is the upper limitation of Br composition claimed in the previous work to stabilize $MAPbBr_xI_{3-x}$ material under the light.[50,52,53,58] However, these studies mostly focus on the $MAPbBr_xI_{3-x}$ unfiltered into porous TiO_2 scaffold, which apparently forms smaller sized grain, comparable to the misconstrue produced in the 540 nm $MAPbBr_xI_{3-x}$ thin film in this study. In this circumstance, we use the $MAPbBr_{0.8}I_{2.2}$ thin films with 320 nm and 530 nm as active layer to compare the misconstrues effect on the cell`s photostability. Figure 5.3b shows the photocurrent of these two types of cells at maximum power output point (MPOP) lasting 33 mins. From the results, the cell with the better crystallinity $MAPbBr_{0.8}I_{2.2}$ thin film stays constant photocurrent output during the long-period test. This result does not only give the steady PCE of the stable device, but also provide an important information that the planer $MAPbBr_{0.8}I_{2.2}$ thin film with a larger grain microstructure can stay stabilized during a 30-minute long period under AM 1.5G illumination. Contractively, the photocurrent curves of the cells with 540 nm and 480nm $MAPbBr_{0.8}I_{2.2}$ layer in Figure 5.3d drop dramatically at first, then are both prone to level off to a certain value around 6 mA/cm^2 after 10 min exposure to light.

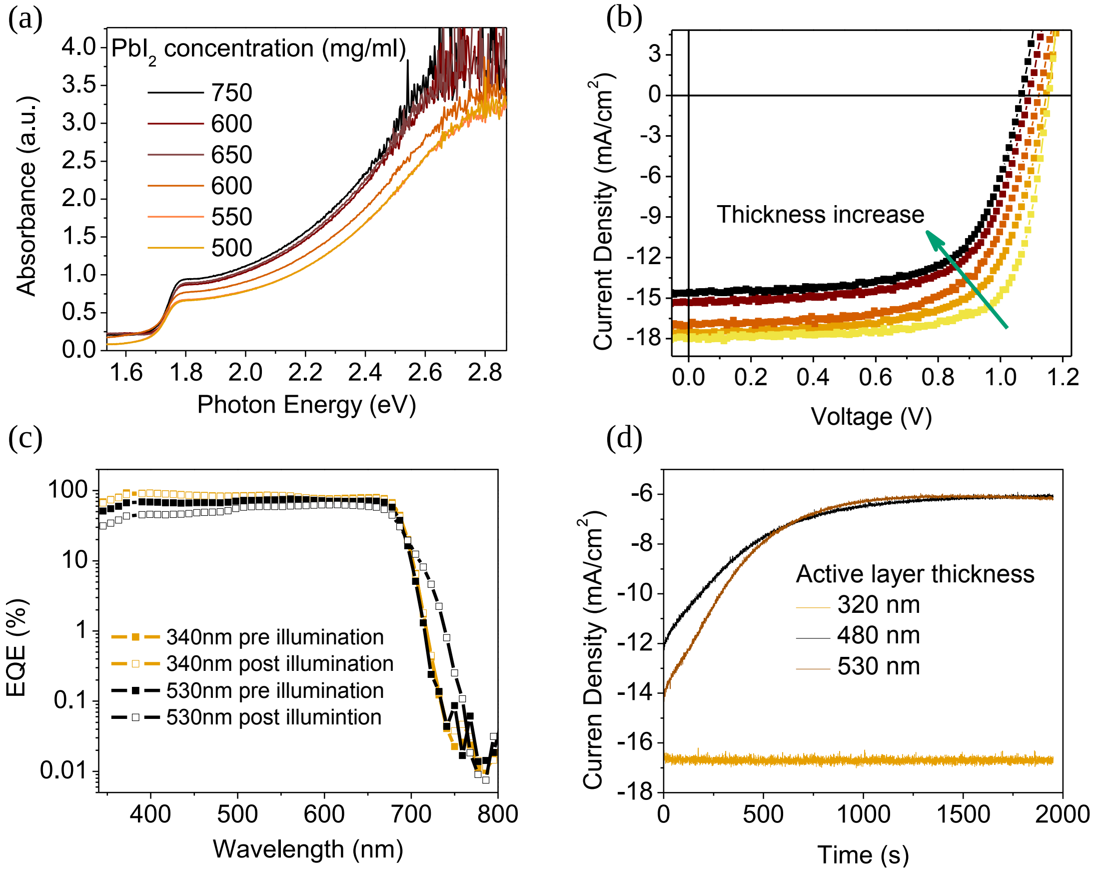

Figure 5.3 (a) Normalized optical absorption spectrum of various thickness of MAPbBr$_{0.8}$I$_{2.2}$; (b) *J-V* curves for optimized solar cells with various thickness of MAPbBr$_{0.8}$I$_{2.2}$ (c) EQE spectra before (square) and after (circle) AM 1.5 G illumination for 20 mins for the MAPbBr$_{0.8}$I$_{2.2}$ cells with 320 nm (orange) and 540 nm (black) MAPbBr$_{0.8}$I$_{2.2}$ film layers; (d) Photocurrent measured for 20 min at the maximum power output point for the three devices with different thickness

5.4 Phase separation in mixed halide WBOTPs

5.4.1 Phase separation observation in EQE measurement of the WBOTP device

It is inferred from the EQE spectrum in Figure 5.3c that a new phase with a certain composition arises gradually after the 10-min exposure to light for the small grain-sized MAPbBr$_{0.8}$I$_{2.2}$. To find out what is the new phase, it is compared the EQE spectrum between the light stable cells and the unstable cells under the circumstances of pre-illumination and post-illumination respectively, shown in Figure 5.3c. For the light stable device with 320 nm $MAPbBr_{0.8}I_{2.2}$, little deviation in EQE profiles between pre illumination and post illumination is presented; while for the unstable device with 540 nm $MAPbBr_{0.8}I_{2.2}$, the EQE degradation is observed after the device was exposed to a similar time of period with to steady photocurrent output test, which agrees with the photocurrent drop in Figure 5.3d. One remarkable point in the unstable cell`s EQE profile (black curve) is that there is a protuberance at the tail of EQE (700nm to 720nm) emerging after the exposure to illumination, and the slope of EQE cutoff for post illumination also decreases from -0. 25 nm^{-1} to -0.29 nm^{-1}. This is anotehr piece of evidence that the active layer of the unstable device become phase separated with the formation of a new I^- rich phase,[59] which contributes the photocurrent output after 700 nm wavelength. In this set of data, the photocurrent decreases more at the short wavelength (350 nm- 550 nm) than the longer wavelength, which indicates the phase separation might occur at the surface to the incident light, where the PTAA and perovskite interface locates. PCBM on the other side of perovskite could passivate the grain boundaries[44,60] which suppresses the halide ion movement among grains for small-range phase separation. Consequently, the new phase formation introduces traps that limits the photogenerated charge transport and collection.

5.4.2 Phase separation observation in other measurements of the WBOTP thin films

The studies above are based on the device performance evolution with the light exposure, which might be decided by the other plausible factors, including the charge recombination, charge diffusion length difference on the $MAPbBr_{0.8}I_{2.2}$ microstructure. To increase the confidence of the conclusion, I investigated the light stability on the naked $MAPbBr_{0.8}I_{2.2}$ thin film. First, I took the X-ray diffraction measurement for the stable $MAPbBr_{0.8}I_{2.2}$ thin film (320nm), and unstable $MAPbBr_{0.8}I_{2.2}$ thin film (540nm). Figure 5.4.2a compares the XRD pattern with normalized intensity for the stable $MAPbBr_{0.8}I_{2.2}$ thin film sample pre-illumination (black) and post-illumination (red); And the same comparison for the unstable counterpart. Within the range of 2theta from 10 degree to 45 degree, we can easily identify the characteristic peaks to cubic Pm-3m group (100), (110), (111), (200), (210) in order, inferring the bravais lattice has already transformed to cubic rather than tetragonal by introducing small amount of bromide.

Comparing XRD pattern of the stable $MAPbBr_{0.8}I_{2.2}$ thin film and the unstable one before illumination, the peaks` position are identical, which agrees with our earlier claim that the composition does not change with the microstructure of $MAPbBr_{0.8}I_{2.2}$ polycrystalline. However, there are more peaks showing up in the XRD pattern for the unstable $MAPbBr_{0.8}I_{2.2}$ than the stable one. Besides, the ratio of (100) peak intensity to other peaks intensity is also higher for the stable $MAPbBr_{0.8}I_{2.2}$. These results suggest that the stable $MAPbBr_{0.8}I_{2.2}$ polycrystalline thin film is better oriented than the unstable one, which confirms the microstructure difference between these two compositional identical thin films. The randomly oriented $MAPbBr_{0.8}I_{2.2}$ contains more incoherent and semi coherent grain boundaries, resulting more lattice strain, thus would enhance the halide migration to assist the phase segregation. By looking into the (200) peak pre and post illumination for the stable $MAPbBr_{0.8}I_{2.2}$ (Figure 5.4.2b) and the unstable $MAPbBr_{0.8}I_{2.2}$ (Figure 5.4.2c), we clearly observed a peak breath for the unstable $MAPbBr_{0.8}I_{2.2}$ after exposure to 3-sun intensity 532nm laser beam for 20 mins. Gaussian fitting is applied to the post-illumination peak (Figure 5.4.2d), from which we can see a small new born peak emerging at 2theta=28.5, where is the (200) peak position for 20% bromide perovskite $MAPbBr_{0.6}I_{2.4}$. This certain composition might be the lowest Gibbs free energy of the alloy, which drives this phase formed automatically with photoexcitation. To exclude the plausible fact that the peak splitting comes from the perovskite decomposition, we put our sample in the dark environment for 2 hours and find the peak splitting can be reversed which is consistent to the former results.[52] The photostability of the $MAPbBr_{0.8}I_{2.2}$ is also supported by the time-evolved photoluminescence (PL) measurement on the naked perovskite shown in Figure 5.4.2e and 5.4.2f. During the 30-minute in-situ observation with 10-sec interval PL collection, it is clear that a lower bandgap phase gradually appears after around 10 mins in Figure 5.4.2e, which is the PL for the unstable $MAPbBr_{0.8}I_{2.2}$.

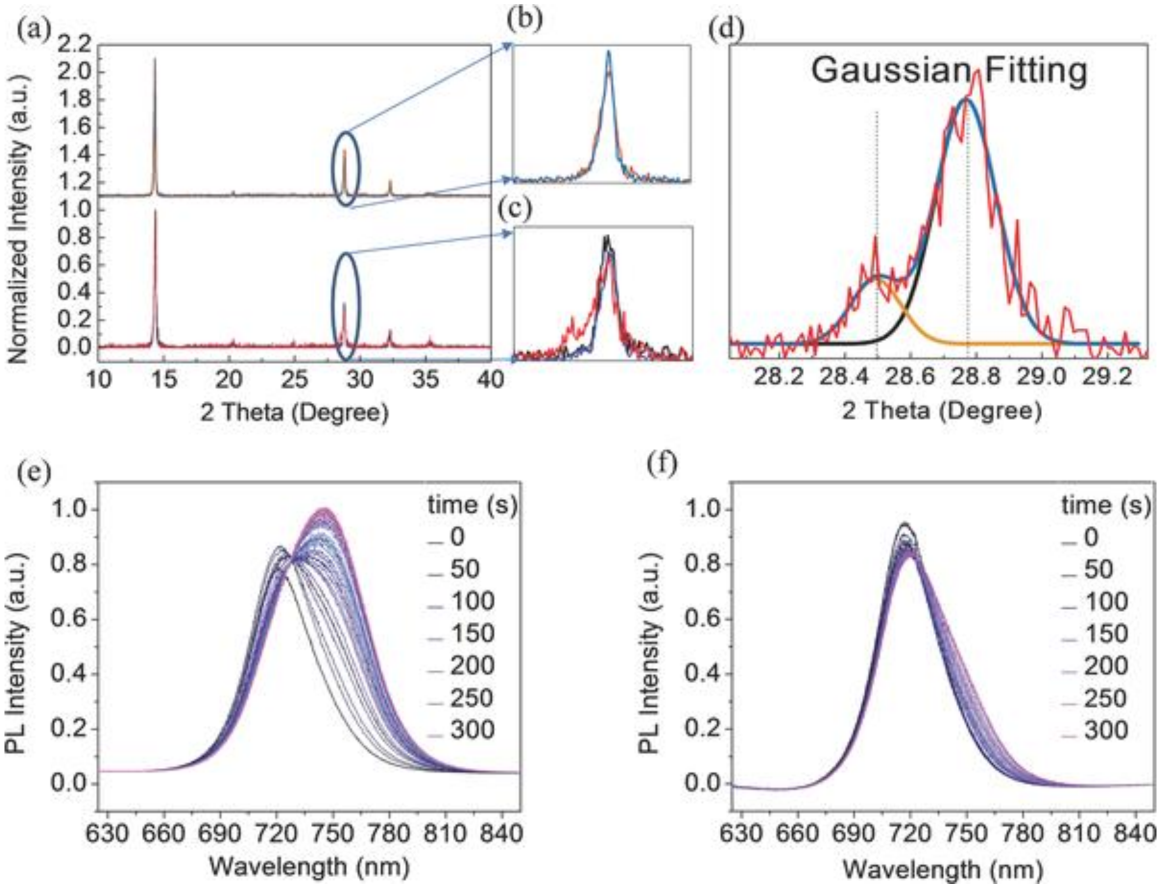

Figure 5.4.2 (a) XRD pattern for $MAPbBr_{0.8}I_{2.2}$ with different perovskite film thickness. b) The (200) XRD peak pre- (black) and post- (red) illumination for the stable $MAPbBr_{0.8}I_{2.2}$ thin film (340 nm). c) The (200) peak before (black) and after (red) exposure to illumination and after recovery (blue) in the dark for 2 hours for the 540 nm $MAPbBr_{0.8}I_{2.2}$ film; d) the Gaussian fitting (red) for (200) peak of the 540 nm $MAPbBr_{0.8}I_{2.}$film after illumination. e–f) PL spectra with an interval of 10 sec for e) the 320 nm $MAPbBr_{0.8}I_{2.2}$ film, and f) the 540 nm $MAPbBr_{0.8}I_{2.2}$ film, measured during illumination of the films under one-sun-intensity 532 nm laser;

To summary, the microstructure of $MAPbBr_{0.8}I_{2.2}$ is demonstrated to be crucial to achieve the stable wide bandgap perovskite solar cells.[47] This explains why the previous large bandgap $MAPbBr_xI_{3-x}$ built on mesoporous scaffold device could not be stable. This work further confirms the potential of planer $MAPbBr_xI_{3-x}$ thin film in the tandem solar cell`s application. Further studies on the role of the grain boundary`s area and grain orientation in phase separation of mixed halide perovskites may contribute to a deeper understanding in this topic.

6 Summary and outlook

To conclude, this thesis demonstrates that bromine-based perovskites exhibits a nonexcitonic nature based on the disparate results from the field dependent EQE of perovskite and excitonic semiconductors. It is further concluded that even though $MAPbBr_3$ (or mixed halide perovskite) have relatively large exciton binding energy in excess of 80 meV, it should still be treated as a nonexcitonic semiconductor. The nonexcitonic nature of metal halide perovskites enables an efficient free charge generation, which explains the outstanding performance of perovskite solar cells. A high performance perovskite photovoltaic device with 1.72 eV bandgap was developed for Si/perovskite tandem solar cell by a low temperature solution process. Hybrid halide was used to enlarge the bandgap by controlling the incorporation of Br into perovskite to obtain 1.72 eV bandgap which was optimized to produce an efficient Si/perovskite tandem solar cell.. Solvent annealing was used to grow large grains, which significantly reduced charge recombination and improved device performance. PCBM passivation was found necessary to achieve the optimized device.

The photostability of the wide-bandgap $MAPbBr_{0.8}I_{2.2}$ devices were demonstrated with a steady photo current output at the maximum power output point over 30 minutes under one sun illumination. Microstructure differences between the photo-stable and photo-unstable devices were presented by the cross-section SEM images of the $MAPbBr_{0.6}I_{2.4}$ active layer showing: the spatial homogeneous polycrystalline with large sized grains and the stacking layered polycrystalline with small sized grains, respectively. The PL and EQE spectral change, accompanied with XRD pattern comparison between the $MAPbBr_{0.8}I_{2.2}$ thin films with two different microstructures, indicate the enhanced crystallinity and grain size are favorable to retain the homogeneous phase for the mixed halide perovskite during the photoexcitation, thus maintain a stable photocurrent output under the device working condition.

In the previous four chapters, I systematically summarized my work concerning the WBOTPs in my Master program. Although some of the results answered the fundamental questions such as the excitonic properties of WBOTPs, the stabilities of WBOTPs, there are still numerous areas to be explored as future work:

First, there is still no exact phase diagram for the bromide and iodide mixed halide perovskite to direct people form phase stable alloys. This is challenging because WBOTPs are organo-inorganic hybrid materials which are difficult to identify the exact components. It is still to be determined if this material has a eutectic point.

Second, in the planar structure, it is hard to form uniform pin hole free WBOTPs to guarantee a high yield of working device without current leakage, though fullerene derivatives might be better or cheaper option in this structure.

Third, if we want to continue to enlarge the bandgap of mixed halide perovskite beyond 1.72 V, no effective fabrication process has been determined preserve the stability of the material under long term light exposure. This needs to be further studied in combination with exploring if a phase diagram of this alloy can be determined6.

7 Reference

1 Park, N.-G. Organometal Perovskite Light Absorbers Toward a 20% Efficiency Low-Cost Solid-State Mesoscopic Solar Cell. *The Journal of Physical Chemistry Letters* **4**, 2423-2429, doi:10.1021/jz400892a (2013).

2 Burschka, J. *et al.* Sequential deposition as a route to high-performance perovskite-sensitized solar cells. *Nature* **499**, 316-319, doi:10.1038/nature12340 (2013).

3 Liu, M., Johnston, M. B. & Snaith, H. J. Efficient planar heterojunction perovskite solar cells by vapour deposition. *Nature* **501**, 395-398, doi:10.1038/nature12509 (2013).

4 Lee, M. M., Teuscher, J., Miyasaka, T., Murakami, T. N. & Snaith, H. J. Efficient Hybrid Solar Cells Based on Meso-Superstructured Organometal Halide Perovskites. *Science* **338**, 643-647, doi:10.1126/science.1228604 (2012).

5 Abrusci, A. *et al.* High-Performance Perovskite-Polymer Hybrid Solar Cells via Electronic Coupling with Fullerene Monolayers. *Nano Letters* **13**, 3124-3128, doi:10.1021/nl401044q (2013).

6 Hodes, G. Perovskite-Based Solar Cells. *Science* **342**, 317-318, doi:10.1126/science.1245473 (2013).

7 Noh, J. H., Im, S. H., Heo, J. H., Mandal, T. N. & Seok, S. I. Chemical management for colorful, efficient, and stable inorganic–organic hybrid nanostructured solar cells. *Nano Letters* **13**, 1764-1769 (2013).

8 Tan, Z.-K. *et al.* Bright light-emitting diodes based on organometal halide perovskite. *Nature nanotechnology* **9**, 687-692 (2014).

9 Albrecht, S. *et al.* Monolithic perovskite/silicon-heterojunction tandem solar cells processed at low temperature. *Energy & Environmental Science* **9**, 81-88 (2016).

10 Todorov, T., Gershon, T., Gunawan, O., Sturdevant, C. & Guha, S. Perovskite-kesterite monolithic tandem solar cells with high open-circuit voltage. *Applied Physics Letters* **105**, 173902 (2014).

11 Löper, P. *et al.* Organic–inorganic halide perovskite/crystalline silicon four-terminal tandem solar cells. *Physical Chemistry Chemical Physics* **17**, 1619-1629 (2015).

12 Hoke, E. T. *et al.* Reversible photo-induced trap formation in mixed-halide hybrid perovskites for photovoltaics. *Chemical Science* **6**, 613-617 (2015).

13 Hu, M. *et al.* Distinct exciton dissociation behavior of organolead trihalide perovskite and excitonic semiconductors studied in the same system. *small* **11**, 2164-2169 (2015).

14 Sheng, C. *et al.* Exciton versus free carrier photogeneration in organometal trihalide perovskites probed by broadband ultrafast polarization memory dynamics. *Physical review letters* **114**, 116601 (2015).

15 Zhen, F. *et al.* Ferroelectricity of CH3NH3PbI3 Perovskite. *The Journal of Physical Chemistry Letters* **6**, 1155-1161, doi:10.1021/acs.jpclett.5b00389 (2015).

16 Green, M. A., Ho-Baillie, A. & Snaith, H. J. The emergence of perovskite solar cells. *Nat Photon* **8**, 506-514, doi:10.1038/nphoton.2014.134 (2014).

17 Even, J., Pedesseau, L., Jancu, J.-M. & Katan, C. Importance of Spin–Orbit Coupling in Hybrid Organic/Inorganic Perovskites for Photovoltaic Applications.

The Journal of Physical Chemistry Letters **4**, 2999-3005, doi:10.1021/jz401532q (2013).

18 Poglitsch, A. & Weber, D. Dynamic disorder in methylammonium trihalogenoplumbates (II) observed by millimeter-wave spectroscopy. *The Journal of Chemical Physics* **87**, doi:10.1063/1.453467 (1987).

19 Mosconi, E., Quarti, C., Ivanovska, T., Ruani, G. & Angelis, F. Structural and electronic properties of organo-halide lead perovskites: a combined IR-spectroscopy and ab initio molecular dynamics investigation. *Physical Chemistry Chemical Physics* **16**, 16137-16144, doi:10.1039/c4cp00569d (2014).

20 Baikie, T., Barrow, N. S., Fang, Y. & Keenan, P. J. A combined single crystal neutron/X-ray diffraction and solid-state nuclear magnetic resonance study of the hybrid perovskites CH 3 NH 3 PbX 3 (X= I, Br and Cl). *... Materials Chemistry A*, doi:10.1039/c5ta01125f (2015).

21 Hopfield, J. Theory of the contribution of excitons to the complex dielectric constant of crystals. *Physical Review* **112**, 1555 (1958).

22 Koops, C. On the dispersion of resistivity and dielectric constant of some semiconductors at audiofrequencies. *Physical Review* **83**, 121 (1951).

23 Lin, Q., Armin, A., Nagiri, R. C. R., Burn, P. L. & Meredith, P. Electro-optics of perovskite solar cells. *Nat Photon* **9**, 106-112, doi:10.1038/nphoton.2014.284 (2015).

24 Miyata, A. *et al.* Direct measurement of the exciton binding energy and effective masses for charge carriers in organic-inorganic tri-halide perovskites. *Nat Phys* **11**, 582-587, doi:10.1038/nphys3357 (2015).

25 Kenichiro, T. *et al.* Comparative study on the excitons in lead-halide-based perovskite-type crystals CH3NH3PbBr3 CH3NH3PbI3. *Solid State Communications* **127**, doi:10.1016/s0038-1098(03)00566-0 (2003).

26 Xiao, Z. *et al.* Efficient, High Yield Perovskite Photovoltaic Devices Grown by Interdiffusion of Solution-Processed Precursor Stacking Layers. *Energy Environ. Sci.* **7**, 2619, doi:10.1039/c4ee01138d (2014).

27 J-Perez, E. J. *et al.* Photoinduced Giant Dielectric Constant in Lead Halide Perovskite Solar Cells. *J. Phys. Chem. Lett.* **5**, 2390, doi:10.1021/jz5011169 (2014).

28 Poglitsch, A. & Weber, D. Dynamic disorder in methylammonium trihalogenoplumbates (II) observed by millimeter-wave spectroscopy. *J. Chem. Phys.* **87**, 6373, doi:10.1063/1.453467 (1987).

29 Kojima, A., Teshima, K., Shirai, Y. & Miyasaka, T. Organometal halide perovskites as visible-light sensitizers for photovoltaic cells. *Journal of the American Chemical Society* **131**, 6050-6051 (2009).

30 Tanaka, K. *et al.* Comparative study on the excitons in lead-halide-based perovskite-type crystals CH 3 NH 3 PbBr 3 CH 3 NH 3 PbI 3. *Solid state communications* **127**, 619-623 (2003).

31 Dow, J. D. & Redfield, D. Electroabsorption in semiconductors: the excitonic absorption edge. *Physical Review B* **1**, 3358 (1970).

32 Moses, D., Wang, J., Heeger, A. J., Kirova, N. & Brazovski, S. Singlet exciton binding energy in poly(phenylene vinylene). *Proc. Natl. Acad. Sci. U. S. A.* **98**, 13496-13500, doi:10.1073/pnas.241497098 (2001).

33 Yang, B. *et al.* Solution‐processed fullerene‐based organic Schottky junction devices for large‐open‐circuit‐voltage organic solar cells. *Advanced Materials* **25**, 572-577 (2013).

34 Yuan, Y. *et al.* Efficiency enhancement in organic solar cells with ferroelectric polymers. *Nat Mater* **10**, 296-302 (2011).

35 Charles, L. B. Electric field assisted dissociation of charge transfer states as a mechanism of photocarrier production. *J. Chem. Phys.* **80**, 4157, doi:10.1063/1.447243 (1984).

36 Veldman, D. *et al.* Compositional and electric field dependence of the dissociation of charge transfer excitons in alternating polyfluorene copolymer/fullerene blends. *J. Am. Chem. Soc.* **130**, 7721-7735, doi:10.1021/ja8012598 (2008).

37 Y. Yuan, T. J. R., P. Sharma, S. Poddar, S. Ducharme, A. Gruverman, Y. Yang, J. Huang. Efficiency enhancement in organic solar cells with ferroelectric polymers. *Nat. Mater.* **10**, 296, doi:10.1038/nmat2951 (2011).

38 Yang, B. *et al.* Solution Processed Fullerene Based Organic Schottky Junction Devices for Large Open Circuit Voltage Organic Solar Cells. *Adv. Mater.* **25**, 572-577, doi:10.1002/adma.201203080 (2013).

39 Steffan, C. *et al.* A photophysical study of PCBM thin films. *Chemical Physics Letters*, doi:10.1016/j.cplett.2007.08.005 (2007).

40 Munn, R., Barbara, P. & Piotr, P. Charge-transfer-induced Frenkel exciton splitting in crystalline fullerene. *Phys. Rev. B*, doi:10.1103/PhysRevB.57.1328 (1998).

41 Jacek, J., Stephan, I., Bobby, G. S. & Keiji, M. Modeling Charge Transfer in Fullerene Collisions via Real-Time Electron Dynamics. *J. Phys. Chem. Lett.*, doi:10.1021/jz3004377 (2012).

42 Albrecht, S. *et al.* Towards optical optimization of planar monolithic perovskite/silicon-heterojunction tandem solar cells. *Journal of Optics* **18**, 064012 (2016).

43 Bi, C., Yuan, Y., Fang, Y. & Huang, J. Low‐Temperature Fabrication of Efficient Wide‐Bandgap Organolead Trihalide Perovskite Solar Cells. *Advanced Energy Materials* **5** (2015).

44 Yuchuan, S., Zhengguo, X., Cheng, B., Yongbo, Y. & Jinsong, H. Origin and elimination of photocurrent hysteresis by fullerene passivation in CH3NH3PbI3 planar heterojunction solar cells. *Nature Communications*, doi:10.1038/ncomms6784 (2014).

45 Heo, J. H. *et al.* Efficient inorganic-organic hybrid heterojunction solar cells containing perovskite compound and polymeric hole conductors. *Nat Photon* **7**, 486-491, doi:10.1038/nphoton.2013.80 (2013).

46 Ryu, S. *et al.* Voltage output of efficient perovskite solar cells with high open-circuit voltage and fill factor. *Energy & Environmental Science* **7**, 2614-2618, doi:10.1039/c4ee00762j (2014).

47 Hu, M., Bi, C., Yuan, Y., Bai, Y. & Huang, J. Stabilized Wide Bandgap MAPbBrxI3–x Perovskite by Enhanced Grain Size and Improved Crystallinity. *Advanced Science* (2015).

48 Auer, S. & Frenkel, D. Suppression of crystal nucleation in polydisperse colloids due to increase of the surface free energy. *Nature* **413**, 711-713 (2001).

49 Giles, E. E. *et al.* Formamidinium lead trihalide: a broadly tunable perovskite for efficient planar heterojunction solar cells. *Energy & Environmental Science*, doi:10.1039/c3ee43822h (2014).

50 Jun Hong, N., Sang Hyuk, I., Jin Hyuck, H., Tarak, N. M. & Sang Il, S. Chemical management for colorful, efficient, and stable inorganic-organic hybrid nanostructured solar cells. *Nano letters* **13**, 1764-1769, doi:10.1021/nl400349b (2013).

51 Bi, C., Yuan, Y., Fang, Y. & Huang, J. Low-Temperature Fabrication of Efficient Wide-Bandgap Organolead Trihalide Perovskite Solar Cells. *Advanced Energy Materials* **5**, n/a-n/a, doi:10.1002/aenm.201401616 (2015).

52 Hoke, E. T., Slotcavage, D. J., Dohner, E. R. & Bowring, A. R. Reversible photo-induced trap formation in mixed-halide hybrid perovskites for photovoltaics. *Chemical …*, doi:10.1039/c4sc03141e (2015).

53 Suarez, B. *et al.* Recombination Study of Combined Halides (Cl, Br, I) Perovskite Solar Cells. *The Journal of Physical Chemistry Letters* **5**, 1628-1635, doi:10.1021/jz5006797 (2014).

54 Edri, E., Kirmayer, S., Kulbak, M., Hodes, G. & Cahen, D. Chloride Inclusion and Hole Transport Material Doping to Improve Methyl Ammonium Lead Bromide Perovskite-Based High Open-Circuit Voltage Solar Cells. *The Journal of Physical Chemistry Letters* **5**, 429-433, doi:10.1021/jz402706q (2014).

55 Vandewal, K., Tvingstedt, K., Gadisa, A., Inganäs, O. & Manca, J. V. On the origin of the open-circuit voltage of polymer–fullerene solar cells. *Nature materials* **8**, 904-909 (2009).

56 Todorov, T., Gershon, T. & Gunawan, O. Perovskite-kesterite monolithic tandem solar cells with high open-circuit voltage. *Applied Physics …* (2014).

57 Wen, X., Wang, S., Ding, Y., Wang, Z. L. & Yang, S. Controlled growth of large-area, uniform, vertically aligned arrays of α-Fe2O3 nanobelts and nanowires. *The Journal of Physical Chemistry B* **109**, 215-220 (2005).

58 Sneha, A. K. *et al.* Band-gap tuning of lead halide perovskites using a sequential deposition process. *Journal of Materials Chemistry A*, doi:10.1039/c4ta00435c (2014).

59 Stefaan De, W. *et al.* Organometallic Halide Perovskites: Sharp Optical Absorption Edge and Its Relation to Photovoltaic Performance. *J. Phys. Chem. Lett.*, doi:10.1021/jz500279b (2014).

60 Jixian, X. *et al.* Perovskite-fullerene hybrid materials suppress hysteresis in planar diodes. *Nature Communications* **6**, doi:10.1038/ncomms8081 (2015).

Copyright Acknowledgement

I acknowledge that the work in this thesis has been published in the peer reviewed journals, and reproduced with permission from publishers as listed below:

Bi, C., Yuan, Y., Fang, Y. & Huang, J. Low-Temperature Fabrication of Efficient Wide-Bandgap Organolead Trihalide Perovskite Solar Cells. Advanced Energy Materials 5 (2015).

Hu, M. *et al.* Distinct exciton dissociation behavior of organolead trihalide perovskite and excitonic semiconductors studied in the same system. *small* **11**, 2164-2169 (2015).

Hu, M., Bi, C., Yuan, Y., Bai, Y. & Huang, J. Stabilized Wide Bandgap MAPbBrxI3–x Perovskite by Enhanced Grain Size and Improved Crystallinity. Advanced Science (2015).